Biochar (2022) 4:31
https://doi.org/10.1007/s42773-022-00158-x

ORIGINAL RESEARCH

p-Arsanilic acid decontamination over a wide pH range using biochar-supported manganese ferrite material as an effective persulfate catalyst: Performances and mechanisms

Bin Yao[1] · Xia Chen[1] · Kun Zhou[1] · Zirui Luo[1] · Peipei Li[1] · Zihui Yang[2] · Yaoyu Zhou[1]

Received: 17 January 2022 / Accepted: 13 May 2022

Abstract

Direct chemical oxidation and pure adsorption could not effectively remove *p*-Arsanilic acid (*p*-ASA) and the released inorganic arsenic. Herein, one novel biochar supported $MnFe_2O_4$ (MFB) was synthesized and adopted for *p*-ASA degradation and synchronous adsorption of the generated inorganic arsenic. The MFB/persulfate (PS) system could remain effective under a wide pH range (3.0–9.0), and the released arsenic could be removed simultaneously by MFB. Mechanism investigation revealed that the functional groups of MFB (i.e. O–C=O and C=O), Fe and Mn oxides on MFB all contributed to PS activation. $O_2^{\cdot-}$ and $^1O_2$ were the main reactive oxygen species (ROS) responsible for *p*-ASA degradation, and $^1O_2$ was the predominant ROS. Besides, the MFB possessed superior reusability. Therefore, it is expected to develop a potential method for organic arsenic contaminants removal *via* an oxidation-adsorption process, and the results could also shed light on the better understanding of the PS activation mechanisms.

✉ Yaoyu Zhou
zhouyy@hunau.edu.cn

[1] Hunan International Scientific and Technological Cooperation Base of Agricultural Typical Pollution Remediation and Wetland Protection, College of Resources and Environment, Hunan Agricultural University, Changsha 410128, China

[2] College of Veterinary Medicine, Hunan Agricultural University, Changsha 410128, China

Published online: 01 June 2022

Graphical Abstract

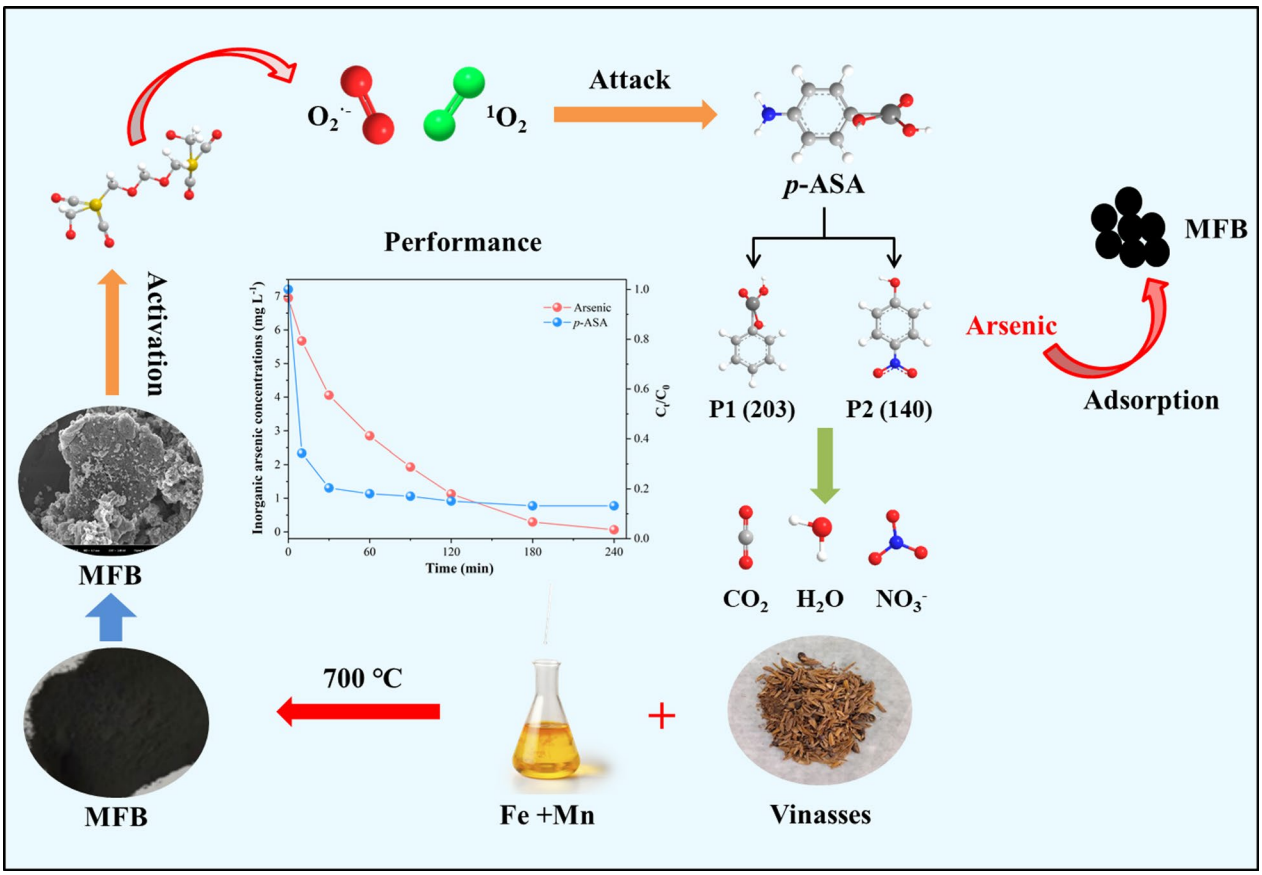

Highlights

- Satisfactory *p*-ASA degradation was achieved in a wide pH range.
- Simultaneous removal of *p*-ASA and the released arsenic was achieved in biochar supported $MnFe_2O_4$/persulfate system.
- Generation abundant reactive oxygen species *via* redox cycles between Mn and Fe.

Keywords Persulfate · Biochar · Manganese ferrite · Redox cycle · Organic arsenic compounds

1 Introduction

As one kind of commonly used phenylarsonic feed additives, *p*-Arsanilic acid (4-aminophenylarsonic acid, *p*-ASA), has been widely applied for promoting growth, guarding diseases, and improving animals' appearance in stock farming (Ke et al. 2021). After ingestion, it is minimally metabolized in animal bodies, and most of them are discharged through excrement with unchanged chemical structure (Chen et al. 2021). Notwithstanding *p*-ASA is low toxic, it could be converted into more mobile and toxic inorganic arsenic (As) species (As(V) and As(III)) *via* biological and abiotic processes once released into the environment (Su et al. 2019; Yao et al. 2021e). As is carcinogenic, and the residual As could pose severe threats to human health (Wang et al. 2020b; Weerasundara et al. 2021). Therefore, developing an effective and environmental-friendly *p*-ASA treatment method for preventing As generation is a top priority.

Presently, adsorption and chemical oxidation have been exploited as two mainstream technologies to remove *p*-ASA from water (Fan et al. 2018; Liang et al. 2021). However, the adsorption removal efficiency was much lower than that towards inorganic arsenic species because of the complicated substituent group of *p*-ASA (Ke et al. 2021). Moreover, although chemical oxidation exhibited desirable degradation performances to *p*-ASA, the generated hazardous inorganic arsenic species should be properly treated (Ye

et al. 2022). Nowadays, the combination of chemical oxidation and adsorption for *p*-ASA elimination has become a trend. Compared with direct adsorption and pure chemical oxidation, the combined technique could effectively decompose *p*-ASA, and the generated inorganic arsenic could be subsequently anchored (Su et al. 2019). Past related research reported that Fenton process was potential for *p*-ASA degradation, and the residual arsenic could be effectively removed through adsorption by the generated precipitate (Xie et al. 2016). But the limitations of narrow pH range and non-reusable Fenton catalysts have hindered its practical application (Yao et al. 2021c).

Up to now, persulfate-based advanced oxidation process has become a research hotspot because of the advantages of strong oxidation ability and broad pH application range (Wu et al. 2020a). Persulfate (PS) could be activated to form powerful reactive oxygen species (ROS) to decompose target pollutants (Huang et al. 2019; Yao et al. 2021a, 2021d). Of late, Fe(II)/PS system has been demonstrated effective for simultaneous *p*-ASA and the formed arsenic removal at pH 6–7 (Wang et al. 2020b). To solve the problem of the generated large amounts of iron sludge, Chen et al. developed Fe^0/PS system to degrade *p*-ASA (Chen et al. 2021). However, Fe^0 preparation was complicated (Yao et al. 2021e). Additionally, Fe^0 is unstable when in contact with air, resulting in a significant decrease of the reactivity (Hussain et al. 2017).

Most recently, magnetic spinel ferrites (MFe_2O_4, M=Cu, Ni, Zn, etc.) with fascinating physiochemical characteristics, including low toxicity, strong magnetism, stability, and high catalytical properties, have been widely deemed as one promising PS activator (Yao et al. 2021a). Chen et al. applied $CuFe_2O_4$ to catalyze peroxymonosulfate for *p*-ASA degradation, and they found that the synchronous removal of p-ASA and the generated arsenic could be achieved (Chen et al. 2020). Nevertheless, some inherent disadvantages, such as agglomeration, non-recyclability, and limited electron transfer, have impeded its reactivity (Wen et al. 2021). To overcome the drawbacks mentioned above, immobilizing spinel ferrites onto different carriers is a preferred choice (Fu et al. 2021; Yao et al. 2021a). Biochar (BC) has been widely reported as a promising support matrix with the advantages of porous structure and huge surface areas (Delgado et al. 2020; Luo et al. 2022; Park et al. 2020; Qiu et al. 2021a; Wu et al. 2020a; Yao et al. 2021b). Our preliminary research reported that the application of biochar could stabilize magnetic ferrites, the behavior of BC is distinct from common carriers, biochar/magnetic ferrite composites could inherit the advantages of biochar and ferrites (Yao et al. 2021a).

As one typical magnetic spinel ferrite, the latest studies have proved that $MnFe_2O_4$ is a desirable PS catalyst (Liu et al. 2021; Ma et al. 2019). Besides, past researches reported that $MnFe_2O_4$ was also an efficient adsorbent both towards organic and inorganic arsenic species (Hu et al. 2017). Furthermore, BC supported $MnFe_2O_4$ nanocomposite has been applied as high-performance adsorbent for several organic arsenic compounds including *p*-ASA (Wen et al. 2021). However, BC supported $MnFe_2O_4$ has never been used as PS activator for *p*-ASA degradation before. If the BC supported $MnFe_2O_4$ could act both as a PS activator for *p*-ASA degradation and as an adsorbent for the released arsenic removal, it is more conducive. Additionally, there are still a number of uncertainties in using BC supported ferrites for PS activation. What kinds of reactive species involved in pollutants degradation are still disputable. Consequently, the catalytic oxidation mechanisms of *p*-ASA using BC supported ferrites need to be further investigated.

In this study, a novel BC supported manganese ferrite (BC@$MnFe_2O_4$, MFB) was prepared using vinasses as raw material. The as-synthesized MFB was applied as PS activator to degrade *p*-ASA, and the released arsenic removal performance in this system was also examined. The main purposes of this research were to (i) develop an innovative PS catalyst for *p*-ASA degradation, (ii) explore the effects of crucial influencing factors on *p*-ASA degradation, (iii) investigate the *p*-ASA removal mechanisms, and (iv) evaluate the synchronous removal performances of the released inorganic arsenic species. Accordingly, this research could provide a promising method for organic arsenic contaminants removal. Besides, the research results could also shed light on better understanding the mechanisms of PS activation.

2 Materials and methods

2.1 Materials and reagents

Vinasses were obtained from Jiugui Liquor Co., Ltd. *p*-ASA ($C_6H_8AsNO_3$, 98%) was purchased in TCI (Shanghai) Development Co., Ltd., $MnSO_4{\cdot}H_2O$, (99.7%), $FeCl_3{\cdot}6H_2O$ (99.7%), 4-(dimethyl amine)benzaldehyde ($C_9H_{11}NO$, 99%), and methanol (CH_4O, ≥ 99.5%, MeOH) were bought from Sinopharm Chemical Reagent Co., Ltd. $Na_2S_2O_8$ (99.99%), *p*-benzoquinone ($C_6H_4O_2$, BQ), and L-Histidine ($C_6H_9N_3O_2$) were bought from Shanghai Macklin Biochemical Co., Ltd.

2.2 Preparation of catalyst

MFB preparation method has been reported in our previous work (Xiang et al. 2020). Briefly, vinasses were washed several times and then naturally dried. Afterwards, 5.0 g of vinasses were added to the mixed solution (100 mL) containing $MnSO_4{\bullet}H_2O$ (0.2 M) and $FeCl_3{\bullet}6H_2O$ (0.4 M), magnetically stirred for 30 min at room temperature (200 rpm).

Subsequently, NaOH (5 M) was added dropwise under stirring to adjust the pH to 10. After heating in an oven at 60 ℃ for 4 h, the suspension was filtered, washed, and dried. Then, the dried solids were placed in a tube furnace and pyrolyzed at 700 ℃ (5 ℃/min) under N_2 conditions for 1 h. Finally, the obtained samples were cooled naturally, grinded, and then sieved into 0.15 mm.

2.3 Characterization and analysis

Scanning electron microscope (SEM, Zeiss Gemini300) integrated with energy-dispersive spectrometry (EDS, Oxford X-MAX) and transmission electron microscope (TEM, FEI TF20) were adopted for surface morphology and elemental compositions analysis. Pore characteristics and specific surface areas were measured by using N_2 adsorption–desorption detection (Quantachrome AUTOSORB IQ). X-ray diffraction (XRD, SmartLab SE) was applied to characterize the crystalline structure of the catalyst. The functional groups were analyzed by Fourier infrared spectroscopy (FTIR, Thermo Scientific Nicolet iS5). The chemical composition of catalyst was determined by X-ray photoelectron spectroscopy (XPS, EscaLab Xi+). *p*-ASA was measured by UV–VIS spectrophotometer (UV1900) using the 4-(dimethylamino)benzaldehyde spectrophotometer method at 450 nm (Wu et al. 2020b). The degradation intermediates were determined by LC–MS. The generated inorganic arsenic species were analyzed with ICP-OES (Agilent 5110).

2.4 Experimental procedure

In a typical experimental procedure, 50 mL of *p*-ASA solution (20 mg/L), certain amounts of PS and catalysts were added in 100 mL plastic bottles to initiate reaction (sharking rate 200 rpm). Samples were taken at given time interval, filtered and detected by UV–VIS. Reactions were performed at different PS concentrations (0–8.4 mM), dosages (0–0.12 g/L), pH values (3.0–9.0), and reaction temperatures (298–318 K) to investigate the wide application range of the as-synthesized catalyst. Solution pH was kept using NaOH and HCl. All experiments were done in duplicates or triplicates.

3 Results and discussion

3.1 Characterization of catalyst

Morphological structures of as-synthesized catalysts were analyzed by SEM and TEM. As presented in Fig. 1a, BC showed rough surface with hierarchical porous structure, which indicated that it was a desirable substrate for $MnFe_2O_4$ nanoparticles supporting. As seen from Fig. 1b, MFB consisted of abundant small solid particles with irregular structure, suggesting that the $MnFe_2O_4$ nanoparticles were successfully loaded on BC. The microstructures of MFB were further explored using TEM. Apparently, $MnFe_2O_4$ nanoparticles were uniformly dispersed on the MFB surface (Fig. 1c). Besides, the lattice fringe spacing in MFB was 0.25 nm, corresponding to the (400) crystal plane of $MnFe_2O_4$ (Yang et al. 2022). Furthermore, the EDS and elemental mapping results demonstrated the presence of C, O, Fe, and Mn on MFB surface (Fig. 1e).

XRD patterns are illustrated in Fig. 2a. Obviously, BC had the broad peak around 22°, which was indexed to amorphous carbon (Yang et al. 2020b). Diffraction peaks at 42.5° and 72.9° individually corresponded to the (400) and (533) crystal planes of $MnFe_2O_4$ (JCPDS No. 10–0319), which was in line with HR-TEM results (Yang et al. 2022). Moreover, the peaks at 35.6° (110), 44.6° (200), and 60.0° (224) were assigned to planes of Mn_2O_3, Fe_3O_4, and Mn_2O_3, respectively (Huang et al. 2020).

N_2 adsorption and desorption tests have been conducted to study the porous characteristics and specific surface areas. As seen from Fig. 2b, the isotherms of BC and MFB all belong to type IV isotherms, indicating that BC and MFB were mainly composed of mesopores (Yang et al. 2022). MFB (97.83 m^2/g) exhibited a higher BET specific surface area than BC (9.82 m^2/g) (Supporting Information), which could be attributed to the $MnFe_2O_4$ adhesion (Rong et al. 2019). The average pore diameters of BC and MFB were in the range of 2–50 nm, demonstrating the formation of mesopores (Feng et al. 2021). The total pore volume of MFB (0.16 cm^3/g) was about 10 times as large as that of BC. Generally, larger specific surface area and abundant pore structures could not only facilitate the PS and pollutants transport, but also be favorable for providing more active sites (Feng et al. 2021; Liu et al. 2021). Thus, MFB was more promising for PS activation contrast to BC.

For more insight into the functional groups of the as-synthesized MFB and BC, FTIR analysis was conducted with the results exhibited in Fig. 2c. In the FTIR spectrum of the pristine BC, three bonds located at 3435 cm^{-1} (–OH) (Li et al. 2019a), 1097 cm^{-1} (C–O) (Huang et al. 2022), and 800–870 cm^{-1} (aromatic C–H) (Yang et al. 2020a) were observed. Compared with the BC, and the peak at 571 cm^{-1} was attributed to Fe–O stretching vibration (Wang et al. 2020a), the peak centered at 463 cm^{-1} corresponded to Mn–O group (Yang et al. 2019), implying the formation of $MnFe_2O_4$ nanoparticles in MFB. To further verify that $MnFe_2O_4$ nanoparticles were successfully loaded into the biochar substrate, the MFB was

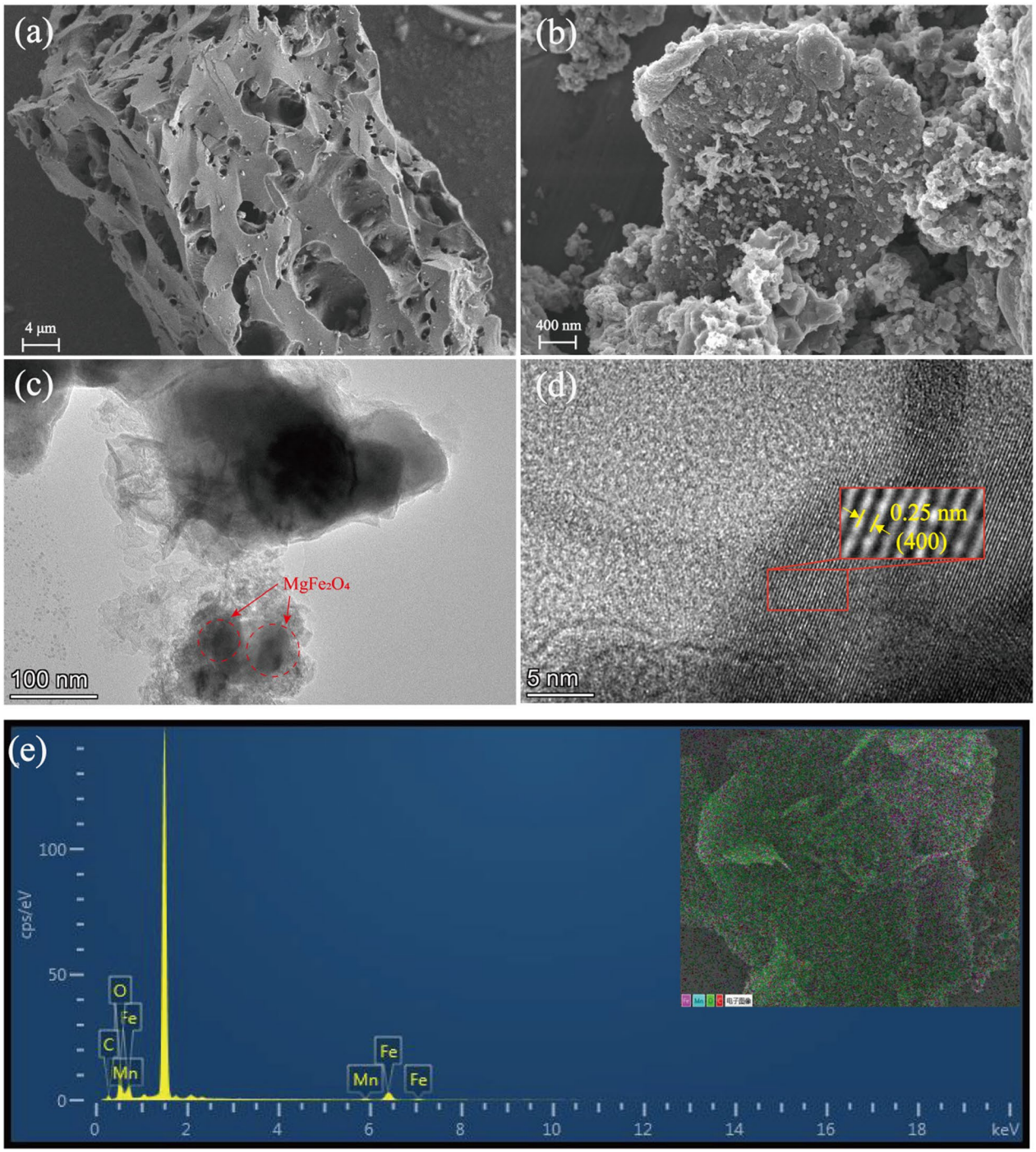

Fig. 1 SEM images of BC (**a**) and MFB (**b**), TEM (**c**) and high-resolution TEM (HR-TEM) images of MFB (**d**), EDS spectrum and elemental mappings of MFB (**e**)

characterized by XPS (Fig. 2d). The results indicated that the BC mainly contains C and O elements, while the main elements existing in the MFB were C, O, Fe and Mn. In summary, all of these characterization results confirmed that the biochar supported $MnFe_2O_4$ composite has been successfully synthesized.

3.2 Degradation of *p*-ASA in different systems

p-ASA degradation performances were evaluated in different reaction systems. Only 16.26% of *p*-ASA was removed with PS alone, suggesting that PS is stable and pure PS could hardly degrade *p*-ASA (Fig. 3a). Approximately 33.05%

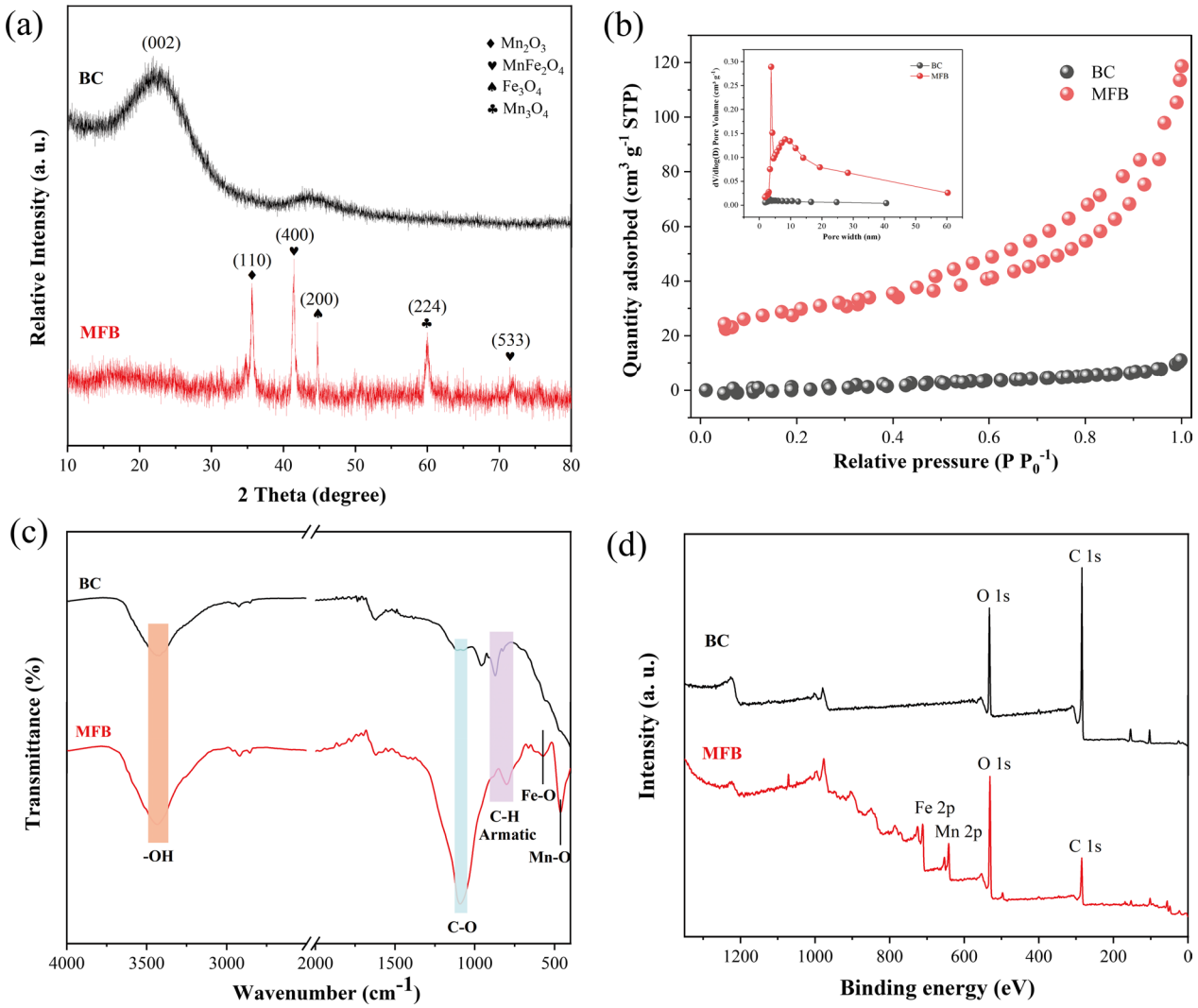

Fig. 2 XRD patterns of BC and MFB (**a**), N_2 sorption isotherms of BC and MFB, insert was the corresponding pore size distribution of BC and MFB (**b**), FTIR spectra of BC and MFB (**c**), XPS spectra of BC and MFB (**d**)

of *p*-ASA was removed with the addition of MFB, which implied that it is difficult to remove *p*-ASA *via* adsorption only. In contrast, the removal efficiency in the MFB/PS system was significantly improved, and 85.28% of *p*-ASA was decomposed after reaction. Moreover, the calculated rate constant (k_{obs}) of *p*-ASA by MFB/PS system enhanced 9.75 times and 3.90 times compared with that by pure PS and MFB alone, respectively. The results demonstrated that the synergistic effects between MFB and PS for removing *p*-ASA, and indicating that MFB was potential to catalyze PS to degrade *p*-ASA (Rong et al. 2019).

3.3 Effects of crucial factors on *p*-ASA degradation

Effect of PS concentration was explored with the results shown in Fig. 3b. It could be observed that *p*-ASA removal rate declined to 60.54% and the k_{obs} dropped to 0.47 h^{-1} with PS concentration increasing. The higher PS concentrations had a negative effect on *p*-ASA degradation because more reactive species could be generated with the excessive addition of PS, which would cause the scavenging of reactive species (Li et al. 2019a). In addition, excessive PS could also lead to the over-occupied active sites of MFB , thus influencing the *p*-ASA degradation (Yu et al. 2019).

The removals of *p*-ASA under different MFB dosages were examined as well. As seen from Fig. 3c, *p*-ASA degradation rate increased from 48.37% to 90.30% as the increasing dosage of MFB from 0.2 g/L to 1.2 g/L. This might be due to the fact that more active sites were provided when more MFB were added (Chen et al. 2021). Additionally, the adsorption removal of *p*-ASA could also been enhanced with the increase of catalyst amounts (Li et al. 2019a).

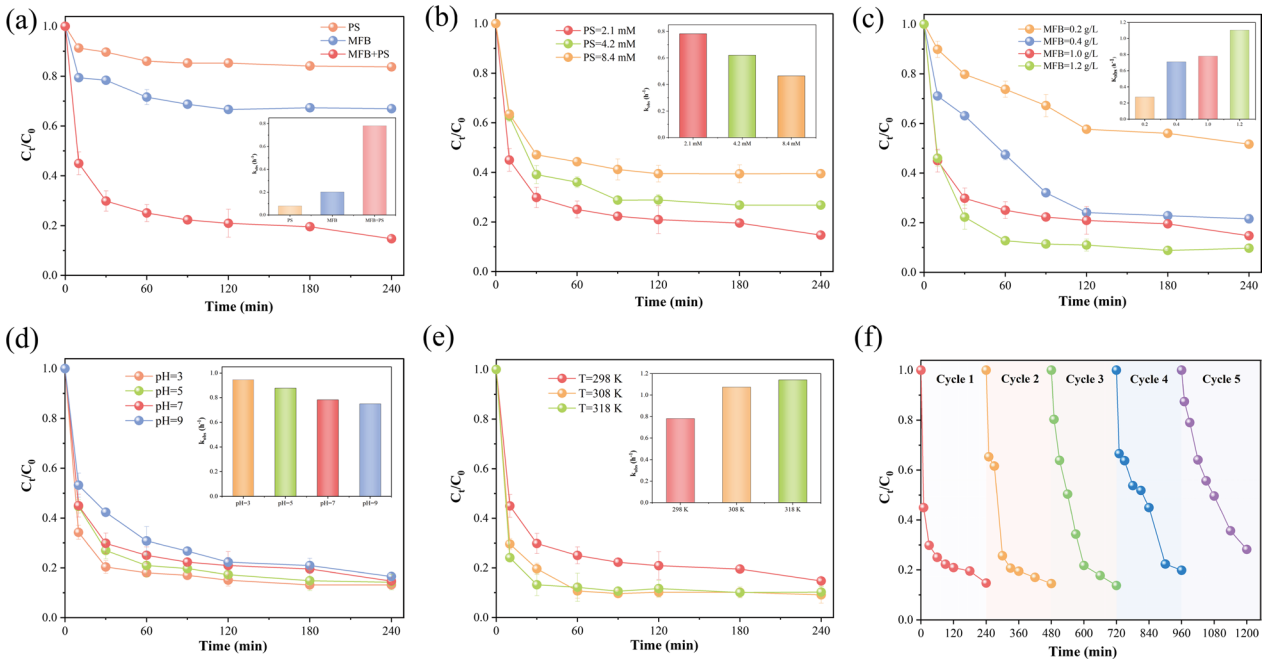

Fig. 3 *p*-ASA degradation efficiencies by BC, and MFB (**a**), *p*-ASA degradation by MFB under different pH (**b**), PS concentrations (**c**), MFB dosages (**d**), reaction temperatures (**e**), and reusability of MFB (**f**). Inserts were the corresponding pseudo-first-order rate constants. Reaction conditions: catalyst = 0–1.2 g/L, PS = 0–8.4 mM, pH = 3–9, T = 298 K–318 K

p-ASA degradation experiments were conducted under different initial pH to test the catalytic performances of the newly developed PS activator. After 240 min, the degradation rate at the pH of 3.0, 5.0, 7.0, 9.0 was 86.85%, 85.77%, 85.28%, and 83.45%, respectively (Fig. 3d). This finding implied that MFB/PS system could remain effective under wide pH range. Besides, the maximum k_{obs} in the system was reached under pH = 3.0 (0.95 h^{-1}), and it gradually declined to 0.75 h^{-1} with an increase of pH from 3.0 to 9.0. Clearly, *p*-ASA degradation was more favorable under the acidic condition, and it might be attributed to the following two reasons. The first one, the Fe/Mn oxides might be leached from MFB at acidic condition, and the generated metal ions could act as catalyst for PS activation (Li et al. 2022). The second one, the electrostatic interactions between MFB and *p*-ASA could also be affected by the variation of solution pH (Li et al. 2019a).

Reaction temperature is another key influencing factor, and Fig. 3e displayed the effect of reaction temperature on *p*-ASA degradation. *p*-ASA degradation rates improved with the increasing reaction temperature. However, the enhancement was not obvious when the reaction temperature further increased from 308 to 318 K. The result was in accordance with the previous study (Huang et al. 2021). This phenomenon was mainly because PS decomposition could be accelerated with elevated reaction temperature, thus promoting the generation of reactive species (Hayat et al. 2019).

3.4 Identification of reactive species

According to the past published studies, the highly effective degradation capacity of PS-based AOPs could be attributed to the formed ROS (Yao et al. 2021a; Yu et al. 2020). To figure out what kinds of ROS were involved in the MFB/PS system, and which kinds of ROS dominated the degradation, quenching analyses using three different types of scavengers (MeOH, BQ, and L-Histidine) were carried out (Yao et al. 2021a). MeOH was applied for quenching ·OH and $SO_4^{\cdot-}$, since it had high reaction rate constants for ·OH ($k = 2.5 \times 10^7$ M^{-1} s^{-1}) and $SO_4^{\cdot-}$ ($k = 9.7 \times 10^8$ M^{-1} s^{-1}) (Zhou et al. 2021), BQ was selected as $O_2^{\cdot-}$ scavenger ($k = 1.0 \times 10^9$ M^{-1} s^{-1}) (Tang et al. 2018). and L-Histidine was applied as $^1O_2$ quencher ($k = 3.0 \times 10^7$ M^{-1} s^{-1}) (Dai et al. 2022). As presented in Fig. 4a, there was no obvious inhibition effect after adding MeOH, suggesting that only small amounts of ·OH and $SO_4^{\cdot-}$ were generated and the roles of ·OH and $SO_4^{\cdot-}$ were negligible. The results were consistent with previous reports (Huang et al. 2022; Meng et al. 2020). Contrarily, the introduction of BQ and L-Histidine remarkably restrained the degradation, and the k_{obs} decreased from 0.78 h^{-1} to 0.37 h^{-1} and 0.22 h^{-1}, respectively. These data demonstrated that $O_2^{\cdot-}$ and $^1O_2$ were the main ROS in the MFB/PS system. Furthermore, the relative contributions of these two kinds of reactive species in the degradation process were assessed based on the following equations

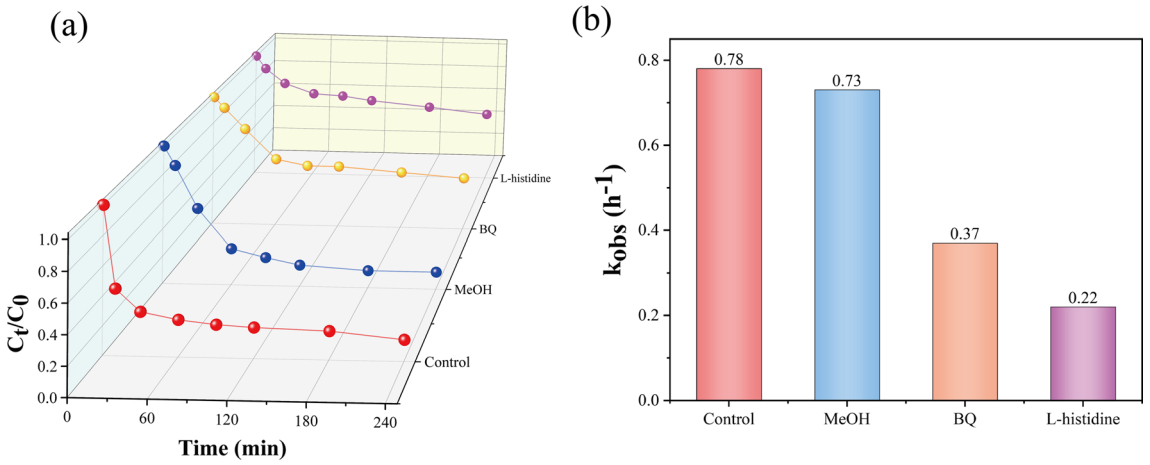

Fig. 4 Effects of different quenchers on *p*-ASA degradation (**a**), and the corresponding changes of reaction rate constants (**b**). Reaction conditions: MFB = 1.0 g/L, PS = 2.1 mM, MeOH = 2.1 M, BQ = 1 mM, L-Histidine = 10 mM, pH = 7.0, T = 298 K

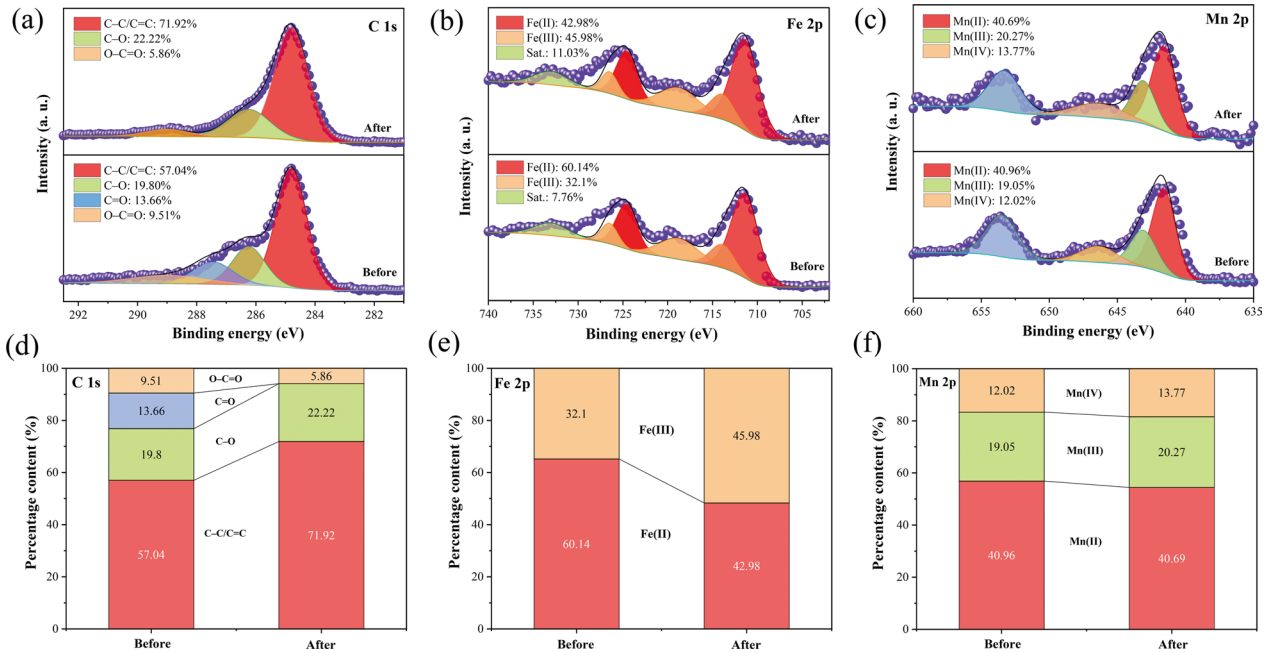

Fig. 5 XPS spectra of C 1 s (**a**), O 1 s (**b**), Fe 2p (**c**), and Mn 2p (**d**) before and after reaction, Percentage contents of C 1s (**e**), O 1s (**f**), Fe 2p (**g**), and Mn 2p (**h**)

(Eqs. (1)–(2)) (Chen et al. 2021). These equations were derived from the differences of rate constants. After calculation, the relative contributions of $O_2^{\cdot-}$ and $^1O_2$ were 52.56% and 71.79%, respectively. Therefore, it could be assumed that $^1O_2$ was the predominant reactive species involved in *p*-ASA degradation.

$$\text{Relative contribution of } O_2^{\cdot-}(\%) = \frac{k_{obs} - k_{obs\,(BQ)}}{k_{obs}} \times 100\% \quad (1)$$

$$\text{Relative contribution of } {}^1O_2(\%) = \frac{k_{obs} - k_{obs\,(L\text{-}Histidine)}}{k_{obs}} \times 100\% \quad (2)$$

where k_{obs} is the reaction rate constant (h^{-1}) in the MFB/PS system, $k_{obs\,(BQ)}$ is the reaction rate constant (h^{-1}) after BQ was added, and $k_{obs\,(L\text{-}Histidine)}$ is the reaction rate constant (h^{-1}) after L-Histidine was injected.

3.5 Investigation of active sites

To further explore the active sites involved in PS activation, XPS analyses of the MFB before and after reaction were carried out. XPS spectra of C 1 s, Fe 2p, and Mn 2p are depicted in Fig. 5. For C 1s spectrum of the MFB before the reaction, four peaks, including C–C/C=C (284.80 eV), C–O (286.24 eV), C=O (287.44 eV), and O–C=O (289.0 eV) were divided (Li et al. 2019b; Rong et al. 2019; Yu et al. 2019). As seen from Fig. 5a and d, the percentage contents of these constituents were 57.04%, 19.80%, 13.66%, and 9.51%, respectively. After reaction, the proportion of O–C=O decreased from 9.51% to 5.86%, and the C=O disappeared, indicating that these functional groups might contribute to the activation process. Moreover, the percentage of C–O increased after the reaction, which might be due to the fact that C=O could act as active site for $^1O_2$ formation and it might be transferred to C–O (Li et al. 2022).

Fe 2p spectra are shown in Fig. 5b. Peaks with the binding energies at 711.40 eV and 724.60 eV were assigned to Fe(II) (Wang et al. 2018), whereas the signals at 713.90 eV, 718.80 eV, and 726.50 eV were Fe(III) characteristic (Qiu et al. 2021b). As depicted in Fig. 5b and e, the proportions of Fe(II) decreased from 60.14% to 42.98% after 4 h of reaction. Meanwhile, the percentages of Fe(III) increased from 32.10% to 45.98%. The result demonstrated that Fe(II) might participate in the PS activation and it was oxidized to Fe(III) after the reaction (Xiao et al. 2022). As for Mn 2p spectra (Fig. 5c), it could be divided into three peaks at 641.60 eV, 643.10 eV, and 646.40 eV, corresponding to Mn(II), Mn(III), and Mn(IV), respectively (Qiu et al. 2021b). After being used, the ratio of Mn(II) barely changed, whereas the percentages of Mn(III) and Mn(IV) slightly increased (Fig. 5c and f). These results suggested that Mn(II) and Mn(III) might both act as active sites for PS catalysis to generate ROS. Meanwhile, the generated Mn(IV) and Mn(III) could be reduced by Fe(II) (Eqs. (3) and (4)). Besides, the Fe(III) might also react with Mn(III) to form Fe(II) and Mn(IV) (Eq. (5)) (Cai et al. 2021; Xu et al. 2019).

$$\equiv \mathrm{Mn(III)} + \equiv \mathrm{Fe(II)} \rightarrow \equiv \mathrm{Mn(II)} + \mathrm{Fe(III)} \quad (3)$$

$$\equiv \mathrm{Mn(IV)} + \equiv \mathrm{Fe(II)} \rightarrow \equiv \mathrm{Mn(III)} + \mathrm{Fe(III)} \quad (4)$$

$$\equiv \mathrm{Fe(III)} + \equiv \mathrm{Mn(III)} \rightarrow \equiv \mathrm{Mn(IV)} + \mathrm{Fe(II)} \quad (5)$$

3.6 Degradation routes of *p*-ASA

The degradation intermediates were analyzed by LC–MS. According to the obtained results and the published literature, a possible degradation route of *p*-ASA in the MFB/PS system under pH 7 was proposed (Supporting Information). It was reported that the amino group on the benzene ring was vulnerable to be attacked by the generated ROS, leading to the formation of P1 ($m/z = 203$) (Chen et al. 2021). The As–C bond is another reactive site that is vulnerable to be destroyed by the ROS. Therefore, *p*-ASA could transform into P2 ($m/z = 140$) through oxidization and hydroxylation (Li et al. 2021). Concurrently, the fracture of As–C bond could result in the generation of arsenous acid, and it was further oxidized into arsenic acid by ROS (Chen et al. 2020). Moreover, these by-products were further attacked by ROS to form small molecule organic acid (such as formic acid, etc.) (Wang et al. 2020b). The generated intermediates were eventually transformed to CO_2, H_2O and NO_3^-.

3.7 Simultaneous adsorption removal of inorganic arsenic species

Considering the inorganic arsenic species, which is more toxic compared with organic arsenic compounds, would be released during *p*-ASA degradation because of the As–C rupture (Li et al. 2021), the variations of arsenic concentrations with reaction time in the MFB/PS system were examined (Supporting Information). It is obvious that the concentrations of arsenic decreased sharply along with the reaction time. After 4 h of reaction, the *p*-ASA degradation ratio reached 85.28%, and the removal rate of the generated inorganic arsenic was 99.08% by MFB simultaneously. This result could be due to the fact that the generated inorganic arsenic species were adsorbed by MFB with large specific surface areas (Chen et al. 2021). Moreover, the residual arsenic concentration was 0.064 mg/L, which was lower than the limit level of 0.1 mg/L required by the Discharge Standard of Pollutants for Municipal Wastewater Treatment Plant of China (GB 18918–2002) (Fan et al. 2021). Therefore, the MFB/PS process was potential for *p*-ASA decontamination.

3.8 Mechanism study

Based on the results obtained above, the mechanisms of *p*-ASA degradation and synchronous adsorption removal of the formed inorganic arsenic species were proposed and depicted in Fig. 6. Firstly, *p*-ASA and PS were both adsorbed on the MFB *via* its high specific surface area. The loaded Fe and Mn oxides on MFB, and the functional groups of MFB (O–C=O and C=O) acted as active sites for PS activation (Eqs. (6)–(9)) (Liu et al. 2021). During the activation process, the redox cycles between Mn and Fe led to the generation of abundant ROS (Eqs. (3)–(5)). Secondly, the formed ROS, including $O_2^{\cdot-}$ and $^1O_2$, effectively decomposed *p*-ASA to produce P1, P2, and inorganic arsenic species (H_3AsO_3 and $H_2AsO_4^-$). $^1O_2$ was the predominant reactive species responsible for *p*-ASA degradation. Then, the generated by-products were further attacked by ROS to form small

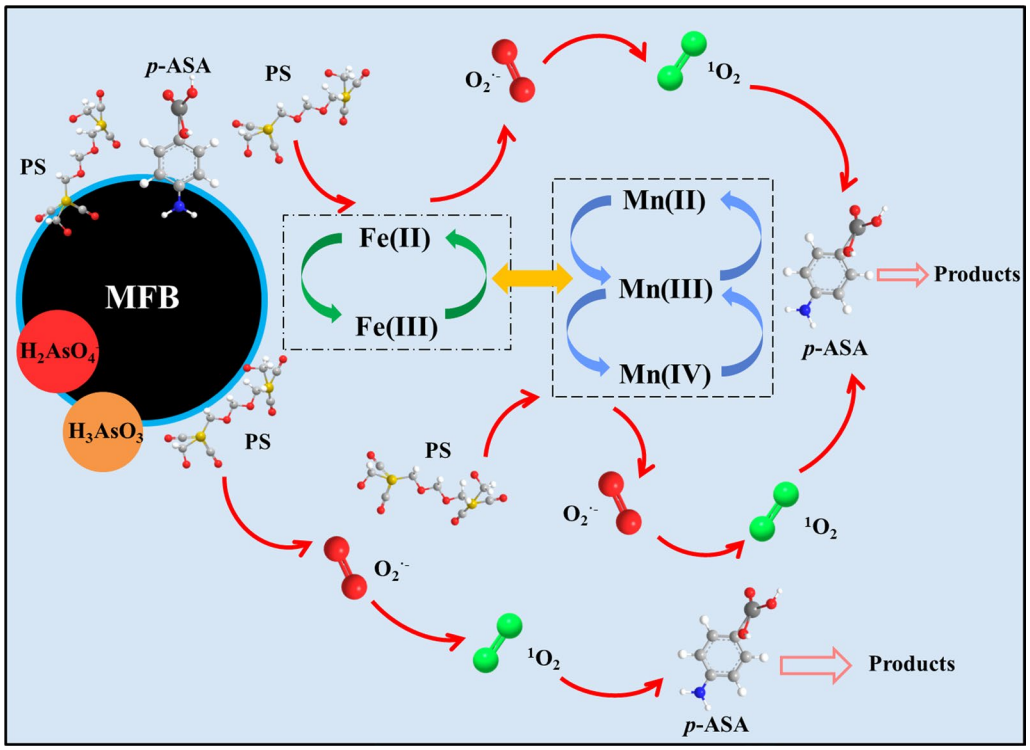

Fig. 6 The mechanisms of *p*-ASA degradation and simultaneous adsorption removal of arsenic in the MFB/PS system

molecule organic acids, which were eventually transformed to CO_2, H_2O and NO_3^-. Concurrently, the released inorganic arsenic species were quickly adsorbed onto the MFB surface. In summary, the mechanism investigation demonstrated our hypothesis that MFB could act both as a PS activator for *p*-ASA effective degradation and as an adsorbent for the released arsenic synchronous removal.

$$S_2O_8^{2-} + 2H_2O \xrightarrow{MFB} HO_2^- + 2SO_4^{2-} + 3H^+ \quad (6)$$

$$HO_2^{\cdot} \xrightarrow{MFB} O_2^{\cdot-} + H^+ \quad (7)$$

$$S_2O_8^{2-} + HO_2^{\cdot} \xrightarrow{MFB} SO_4^{\cdot-} + 2SO_4^{2-} + O_2^{\cdot-} + 3H^+ \quad (8)$$

$$2O_2^{\cdot-} + 2H_2O \xrightarrow{MFB} {}^1O_2 + H_2O_2 + 2OH^- \quad (9)$$

3.9 Reusability of MFB

Reusability of catalyst is of significance for the practical application. Therefore, the cyclic experiments were performed to test MFB's stability. As displayed in Fig. 3f, the *p*-ASA removal ratio slightly decreased to 71.83% in the MFB/PS system after 5 cycles. The result suggested that the MFB was a desirable catalyst for PS activation as well as a high-performance adsorbent for the released arsenic removal, which possessed superior reusability.

4 Conclusions

A novel BC supported $MnFe_2O_4$ (MFB) serving as a PS activator and adsorbent was fabricated for *p*-ASA degradation and synchronous adsorption of the generated arsenic. Approximately 85% of *p*-ASA was degraded in the MFB/PS system in a wide pH range (3.0–9.0) after 4 h of reaction, and the removal rate of the generated inorganic arsenic was 99.08% by MFB simultaneously. The Fe and Mn oxides on

MFB, and the functional groups of MFB (i.e. O–C=O and C=O) might act as active sites for PS activation. Moreover, the redox cycles between Mn and Fe led to the generation of powerful ROS. $^1O_2$ was the predominant ROS responsible for *p*-ASA degradation. The MFB possessed superior reusability. This research developed a potential method for for the removal of organic arsenic contaminants, and it is envisioned to be an environmental-friendly approach for different aqueous contaminants treatment.

Supplementary Information The online version contains supplementary material available at https://doi.org/10.1007/s42773-022-00158-x.

Acknowledgements Not applicable.

Author contributions BY: Conceptualization, methodology, software, visualization, writing—original draft, writing—review and editing. XC: Investigation. KZ: Investigation. ZL: Investigation, Writing—review and editing. PL: Investigation. ZY: Investigation. YZ: Conceptualization, writing—review and editing, supervision. All authors read and approved the final manuscript.

Funding This study was financially supported by the National Natural Science Foundation of China (Grant No. 51709103), Natural Science Foundation of Hunan Province, China (Grant Nos. 2018JJ3242 and 2021JJ30362), Science and Technology Innovation Leading Plan of High Tech Industry in Hunan Province (Grant No. 2021GK4055), Training Program for Excellent Young Innovators of Changsha (Grant No. kq1802020).

Data availability The data that support the findings of this study are available from the corresponding author upon request.

Declarations

Ethics approval and consent to participate Not applicable.

Consent for publication The corresponding author consents on behalf of all the authors that this is original work and has permission to be published.

Competing interests The authors declare that they have no known competing financial interests or personal relationships that could have appeared to influence the work reported in this paper.

References

Cai M, Zhang Y, Dong C, Wu W, Wang Q, Song Z, Shi Y, Wu L, Jin M, Dionysiou DD, Wei Z (2021) Manganese doped iron–carbon composite for synergistic persulfate activation: reactivity, stability, and mechanism. J Hazard Mater 405:124228

Chen S, Deng J, Ye C, Xu C, Huai L, Li J, Li X (2020) Simultaneous removal of para-arsanilic acid and the released inorganic arsenic species by $CuFe_2O_4$ activated peroxymonosulfate process. Sci Total Environ 742:140587

Chen S, Deng J, Ye C, Xu C, Huai L, Ling X, Li J, Li X (2021) Degradation of p-arsanilic acid by pre-magnetized Fe^0/persulfate system: Kinetics, mechanism, degradation pathways and DBPs formation during subsequent chlorination. Chem Eng J 410:128435

Dai C, Li S, Duan Y, Leong KH, Liu S, Zhang Y, Zhou L, Tu Y (2022) Mechanisms and product toxicity of activated carbon/peracetic acid for degradation of sulfamethoxazole: implications for groundwater remediation. Water Res 216:118347

Delgado F, Gutierrez VS, Dennehy M, Alvarez M (2020) Stable and efficient metal-biochar supported catalyst: degradation of model pollutants through sulfate radical-based advanced oxidation processes. Biochar 2(3):319–328

Fan J, Ding Z, Zhao Z, Liu J (2018) Degradation of *p*-arsanilic acid and simultaneous in-situ removal of arsenic species with ferrate(VI): Kinetics, intermediate and degradation pathway. Chem Eng J 350:453–462

Fan Y, Li T, Cun D, Tang H, Dai Y, Wang F, Liang W (2021) Removal of arsenic by pilot-scale vertical flow constructed wetland. Front Environ Sci Eng 15(4):79

Feng D, Guo D, Zhang Y, Sun S, Zhao Y, Shang Q, Sun H, Wu J, Tan H (2021) Functionalized construction of biochar with hierarchical pore structures and surface O-/N-containing groups for phenol adsorption. Chem Eng J 410:127707

Fu D, Kurniawan TA, Li H, Wang H, Wang Y, Li Q (2021) Co-oxidative removal of arsenite and tetracycline based on a heterogeneous Fenton-like reaction using iron nanoparticles-impregnated biochar. Environ Pollut 290:118062

Hayat W, Zhang Y, Hussain I, Du X, Du M, Yao C, Huang S, Si F (2019) Efficient degradation of imidacloprid in water through iron activated sodium persulfate. Chem Eng J 370:1169–1180

Hu Q, Liu Y, Gu X, Zhao Y (2017) Adsorption behavior and mechanism of different arsenic species on mesoporous $MnFe_2O_4$ magnetic nanoparticles. Chemosphere 181:328–336

Huang Q, Song S, Chen Z, Hu B, Chen J, Wang X (2019) Biochar-based materials and their applications in removal of organic contaminants from wastewater: state-of-the-art review. Biochar 1(1):45–73

Huang D, Zhang Q, Zhang C, Wang R, Deng R, Luo H, Li T, Li J, Chen S, Liu C (2020) Mn doped magnetic biochar as persulfate activator for the degradation of tetracycline. Chem Eng J 391:123532

Huang H, Guo T, Wang K, Li Y, Zhang G (2021) Efficient activation of persulfate by a magnetic recyclable rape straw biochar catalyst for the degradation of tetracycline hydrochloride in water. Sci Total Environ 758:143957

Huang P, Zhang P, Wang C, Tang J, Sun H (2022) Enhancement of persulfate activation by Fe-biochar composites: Synergism of Fe and N-doped biochar. Appl Catal B 303:120926

Hussain I, Li M, Zhang Y, Li Y, Huang S, Du X, Liu G, Hayat W, Anwar N (2017) Insights into the mechanism of persulfate activation with nZVI/BC nanocomposite for the degradation of nonylphenol. Chem Eng J 311:163–172

Ke M-K, Huang G-X, Mei S-C, Wang Z-H, Zhang Y-J, Hua T-W, Zheng L-R, Yu H-Q (2021) Interface-promoted direct oxidation of *p*-Arsanilic acid and removal of total arsenic by the coupling of

peroxymonosulfate and Mn-Fe-mixed oxide. Environ Sci Technol 55(10):7063–7071

Li L, Lai C, Huang F, Cheng M, Zeng G, Huang D, Li B, Liu S, Zhang M, Qin L, Li M, He J, Zhang Y, Chen L (2019a) Degradation of naphthalene with magnetic bio-char activate hydrogen peroxide: synergism of bio-char and Fe–Mn binary oxides. Water Res 160:238–248

Li M, Liu H, Chen T, Dong C, Sun Y (2019b) Synthesis of magnetic biochar composites for enhanced uranium(VI) adsorption. Sci Total Environ 651:1020–1028

Li Y, Liu L, Wang Z, Zhou L, Lan Y, Chen C (2021) Simultaneous oxidation of 4-aminophenylarsonic acid and adsorption of the produced inorganic arsenic by a combination of Co_3O_4-La_2CO_5@RSBC with peroxymonosulfate. Chem Eng J 413:127417

Li X, Yu Z, Chen Q, Wang C, Ma L, Shen G (2022) Kill three birds with one stone: Iron-doped graphitic biochar from biogas residues for ammonium persulfate activation to simultaneously degrade benzo[a]pyrene and improve lettuce growth. Chem Eng J 430:132844

Liang L, Xi F, Tan W, Meng X, Hu B, Wang X (2021) Review of organic and inorganic pollutants removal by biochar and biochar-based composites. Biochar 3(3):255–281

Liu Z, Gao Z, Wu Q (2021) Activation of persulfate by magnetic zirconium-doped manganese ferrite for efficient degradation of tetracycline. Chem Eng J 423:130283

Luo Z, Yao B, Yang X, Wang L, Xu Z, Yan X, Tian L, Zhou H, Zhou Y (2022) Novel insights into the adsorption of organic contaminants by biochar: a review. Chemosphere 287:132113

Ma Q, Zhang X, Guo R, Zhang H, Cheng Q, Xie M, Cheng X (2019) Persulfate activation by magnetic γ-Fe_2O_3/Mn_3O_4 nanocomposites for degradation of organic pollutants. Sep Purif Technol 210:335–342

Meng H, Nie C, Li W, Duan X, Lai B, Ao Z, Wang S, An T (2020) Insight into the effect of lignocellulosic biomass source on the performance of biochar as persulfate activator for aqueous organic pollutants remediation: epicarp and mesocarp of citrus peels as examples. J Hazard Mater 399:123043

Park J-H, Wang JJ, Park KH, Seo D-C (2020) Heterogeneous fenton oxidation of methylene blue with Fe-impregnated biochar catalyst. Biochar 2(2):165–176

Qiu M, Hu B, Chen Z, Yang H, Zhuang L, Wang X (2021a) Challenges of organic pollutant photocatalysis by biochar-based catalysts. Biochar 3(2):117–123

Qiu Y, Zhang Q, Wang Z, Gao B, Fan Z, Li M, Hao H, Wei X, Zhong M (2021b) Degradation of anthraquinone dye reactive blue 19 using persulfate activated with Fe/Mn modified biochar: radical/non-radical mechanisms and fixed-bed reactor study. Sci Total Environ 758:143584

Rong X, Xie M, Kong L, Natarajan V, Ma L, Zhan J (2019) The magnetic biochar derived from banana peels as a persulfate activator for organic contaminants degradation. Chem Eng J 372:294–303

Su S, Cao C, Zhao Y, Dionysiou DD (2019) Efficient transformation and elimination of roxarsone and its metabolites by a new α-FeOOH@GCA activating persulfate system under UV irradiation with subsequent As(V) recovery. Appl Catal B 245:207–219

Tang L, Liu Y, Wang J, Zeng G, Deng Y, Dong H, Feng H, Wang J, Peng B (2018) Enhanced activation process of persulfate by mesoporous carbon for degradation of aqueous organic pollutants: electron transfer mechanism. Appl Catal B 231:1–10

Wang L, Wang J, Wang Z, He C, Lyu W, Yan W, Yang L (2018) Enhanced antimonate (Sb(V)) removal from aqueous solution by La-doped magnetic biochars. Chem Eng J 354:623–632

Wang H, Xiao K, Yang J, Yu Z, Yu W, Xu Q, Wu Q, Liang S, Hu J, Hou H, Liu B (2020a) Phosphorus recovery from the liquid phase of anaerobic digestate using biochar derived from iron−rich sludge: a potential phosphorus fertilizer. Water Res 174:115629

Wang P, He X, Zhang W, Ma J, Jiang J, Huang Z, Cheng H, Pang S, Zhou Y, Zhai X (2020b) Highly efficient removal of *p*-arsanilic acid with Fe(II)/peroxydisulfate under near-neutral conditions. Water Res 177:115752

Weerasundara L, Ok Y-S, Bundschuh J (2021) Selective removal of arsenic in water: a critical review. Environ Pollut 268:115668

Wen Z, Xi J, Lu J, Zhang Y, Cheng G, Zhang Y, Chen R (2021) Porous biochar-supported $MnFe_2O_4$ magnetic nanocomposite as an excellent adsorbent for simultaneous and effective removal of organic/inorganic arsenic from water. J Hazard Mater 411:124909

Wu P, Wang Z, Wang H, Bolan NS, Wang Y, Chen W (2020a) Visualizing the emerging trends of biochar research and applications in 2019: a scientometric analysis and review. Biochar 2(2):135–150

Wu S, Yang D, Zhou Y, Zhou H, Ai S, Yang Y, Wan Z, Luo L, Tang L, Tsang DCW (2020b) Simultaneous degradation of *p*-arsanilic acid and inorganic arsenic removal using M-rGO/PS Fenton-like system under neutral conditions. J Hazard Mater 399:123032

Xiang Y, Yang X, Xu Z, Hu W, Zhou Y, Wan Z, Yang Y, Wei Y, Yang J, Tsang DCW (2020) Fabrication of sustainable manganese ferrite modified biochar from vinasse for enhanced adsorption of fluoroquinolone antibiotics: effects and mechanisms. Sci Total Environ 709:136079

Xiao K, Liang F, Liang J, Xu W, Liu Z, Chen B, Jiang X, Wu X, Xu J, Beiyuan J, Wang H (2022) Magnetic bimetallic Fe, Ce-embedded N-enriched porous biochar for peroxymonosulfate activation in metronidazole degradation: applications, mechanism insight and toxicity evaluation. Chem Eng J 433:134387

Xie X, Hu Y, Cheng H (2016) Rapid degradation of *p*-arsanilic acid with simultaneous arsenic removal from aqueous solution using Fenton process. Water Res 89:59–67

Xu X, Yang Y, Jia Y, Lian X, Zhang Y, Feng F, Liu Q, Xi B, Jiang Y (2019) Heterogeneous catalytic degradation of 2,4-dinitrotoluene by the combined persulfate and hydrogen peroxide activated by the as-synthesized Fe-Mn binary oxides. Chem Eng J 374:776–786

Yang F, Zhang S, Cho D-W, Du Q, Song J, Tsang DCW (2019) Porous biochar composite assembled with ternary needle-like iron-manganese-sulphur hybrids for high-efficiency lead removal. Biores Technol 272:415–420

Yang L, Chen Y, Ouyang D, Yan J, Qian L, Han L, Chen M, Li J, Gu M (2020a) Mechanistic insights into adsorptive and oxidative removal of monochlorobenzene in biochar-supported nanoscale zero-valent iron/persulfate system. Chem Eng J 400:125811

Yang Y, Wang R, Ding L, Qu D, Zhang Y, Han Q, Liu N, Piao Y (2020b) Catalytic performance and mechanism of biochars for dechlorination of tetrachloroethylene in sulfide aqueous solution. Appl Catal B 278:119285

Yang X, Zeng L, Huang J, Mo Z, Guan Z, Sun S, Liang J, Huang S (2022) Enhanced sludge dewaterability by a novel $MnFe_2O_4$-Biochar activated peroxymonosulfate process combined with Tannic acid. Chem Eng J 429:132280

Yao B, Luo Z, Du S, Yang J, Zhi D, Zhou Y (2021a) Magnetic $MgFe_2O_4$/biochar derived from pomelo peel as a persulfate activator for levofloxacin degradation: effects and mechanistic consideration. Bioresour Technol 346:126547

Yao B, Luo Z, Du S, Yang J, Zhi D, Zhou Y (2021b) Sustainable biochar/$MgFe_2O_4$ adsorbent for levofloxacin removal: adsorption performances and mechanisms. Biores Technol 340:125698

Yao B, Luo Z, Yang J, Zhi D, Zhou Y (2021c) $Fe^{II}Fe^{III}$ layered double hydroxide modified carbon felt cathode for removal of ciprofloxacin in electro-Fenton process. Environ Res 197:111144

Yao B, Luo Z, Zhi D, Hou D, Luo L, Du S, Zhou Y (2021d) Current progress in degradation and removal methods of polybrominated diphenyl ethers from water and soil: a review. J Hazard Mater 403:123674

Yao B, Zhi D, Zhou Y (2021e) Chapter 10 - Iron-based materials for removal of arsenic from water. In: Núñez-Delgado A (ed) Sorbents materials for controlling environmental pollution. Elsevier, Amsterdam, pp 209–245

Ye C, Deng J, Huai L, Cai A, Ling X, Guo H, Wang Q, Li X (2022) Multifunctional capacity of CoMnFe-LDH/LDO activated peroxymonosulfate for *p*-arsanilic acid removal and inorganic arsenic immobilization: performance and surface-bound radical mechanism. Sci Total Environ 806:150379

Yu J, Tang L, Pang Y, Zeng G, Wang J, Deng Y, Liu Y, Feng H, Chen S, Ren X (2019) Magnetic nitrogen-doped sludge-derived biochar catalysts for persulfate activation: internal electron transfer mechanism. Chem Eng J 364:146–159

Yu J, Tang L, Pang Y, Zeng G, Feng H, Zou J, Wang J, Feng C, Zhu X, Ouyang X, Tan J (2020) Hierarchical porous biochar from shrimp shell for persulfate activation: a two-electron transfer path and key impact factors. Appl Catal B 260:118160

Zhou X, Jawad A, Luo M, Luo C, Zhang T, Wang H, Wang J, Wang S, Chen Z, Chen Z (2021) Regulating activation pathway of Cu/persulfate through the incorporation of unreducible metal oxides: Pivotal role of surface oxygen vacancies. Appl Catal B 286:119914